1 Primitive chain network simulations for the interrupted shear response of entangled polymeric liquids

2

3 Yuichi Masubuchi[1,2]*, Yuya Doi[2] and Takashi Uneyama[1,2]

4 [1]Center of Computational Science, and [2]Department of Materials Physics, Nagoya University, Nagoya

5 4648603, Japan.

6

7 *To whom correspondence should be addressed

8 mas@mp.pse.nagoya-u.ac.jp

9

ABSTRACT

11 The non-linear viscoelastic response under interrupted shear flows is one of the interesting

12 characteristics of entangled polymers. In particular, the stress overshoot in the resumed shear has been

13 discussed concerning the recovery of the entanglement network in some studies. In this study, we

14 performed multi-chain slip-link simulations to observe the molecular structure of an entangled

15 polymer melt. After confirming the reasonable reproducibility of our simulation with the literature

16 data, we analyzed the molecular characteristics following the decoupling approximation. We

17 reasonably found that the segment orientation dominates the stress overshoot even under the resumed

18 shear with minor contributions from the segment stretch and entanglement density. We defined the

19 mitigation function for the recovery of stress overshoot as a function of the rest time and compared it

20 with the relaxation of the molecular quantities after the initial shear. As a result, we have found that

21 the mitigation of stress overshoot coincides with the relaxation of entanglement density.

22

Keywords

24 viscoelasticity, polymers, molecular simulation

25

INTRODUCTION

27 Stress growth under interrupted shear flows is one of the interesting non-linear viscoelastic behaviors

28 of entangled polymers[1,2]. In this rheological test, an equilibrated polymeric liquid is subjected to fast,

29 steady shear. After a certain amount of applied shear, the flow is interrupted to relax the material.

30 During the relaxation, before reaching equilibrium, the material is exposed to the second shear. The

31 material response under the second shear depends on the interval between initial and resumed flows-

32 the so-called rest time. With a sufficiently long rest time, the material equilibrates, and the stress

33 growth under resumed flow is identical to that under the initial flow. More specifically, the stress

34 increases up to a strain of approximately 2 to 3 and shows an overshoot before reaching a steady value.

35 The maximum stress at the overshoot monotonically decreases with decreasing rest time. Because no

36 overshoot occurs in the absence of a rest, the decline of the overshoot is intuitive in a qualitative sense.

37   However, no quantitative explanation has been established.

38

39   In some studies, the mitigation of stress overshoot has been attributed to a structural change of the

40   entanglement network. To our knowledge, network modification under deformation was firstly

41   mentioned by Tobolsky et al.[3,4] according to the transient network idea. Graessley[5] described the shear

42   thinning of polymeric liquids by considering the rates of creation and destruction of entanglements.

43   Doi and Edwards[6] derived the universal damping function under large step shear deformations from

44   the loss of entanglements induced by chain contraction. Similar discussions have been made for

45   interrupted shear[7–11].

46

47   The non-linear response under interrupted shear is not necessarily solely due to modification of the

48   entanglement network. For example, Santangelo and Roland[12] showed that an unentangled

49   polystyrene melt exhibits similar rest time dependence of stress overshoot. They mentioned that the

50   suppression of overshoot is due to the unrelaxed segmental orientation. Even for entangled polymers,

51   orientation contributes to stress, as discussed for the stress overshoot during the initial shear[13–16] on

52   the basis of the stress-optical law. Indeed, Ianniruberto and Marrucci[17] demonstrated that the integral

53   constitutive equation proposed by Doi and Edwards[18] qualitatively reproduces the interrupted shear

54   results reported by Wang et al.[11], even though the model incorporates neither chain stretch nor loss of

55   entanglement. In addition, Graham et al.[19] semi-quantitatively reproduced the data of Wang et al. [11]

56   using a tube model, in which chain stretch is incorporated but the entanglement density is unchanged.

57   Nevertheless, as noted by Ianniruberto and Marrucci[17], further studies are required to discriminate the

58   contributions from orientation, stretch and entanglement density in the stress response under

59   interrupted shear.

60

61   In this study, through the multi-chain slip-link simulation (the so-called primitive chain network (PCN)

62   simulation[20–23]), we investigated the stress response of an entangled polymer melt under interrupted

63   shear flows. The observed stress response was in reasonable agreement with the experimental results

64   of Roy and Roland[24]. We obtained the time development of segmental orientation, stretch, and

65   entanglement density separately. The results demonstrate that, for the stress overshoot, the contribution

66   from the orientation is dominant, whereas the contribution from the entanglement density is minor.

67   Meanwhile, the mitigation of overshoot coincides with the relaxation of entanglement density.

68

69   **MODEL AND SIMULATIONS**

70   Because the model and code used in this study are the same as those used for previous studies[25–29],

71   only a brief description is given here. A melt of entangled polymer was replaced by a network

72   consisting of network nodes, strands and dangling ends. Each polymer chain was represented by a

73 path connecting two dangling ends through the nodes and strands. At each node, a slip-link was

74 positioned to bundle two chains according to the binary assumption of entanglement. The slip-link

75 allows sliding of the bundled chains, and it is destroyed if one of the chains slides off. By contrast,

76 when a chain end protrudes from the connected slip-link by a critical amount, a new slip-link is created

77 on the dangling segment by hooking another strand within a cut-off distance equal to the average

78 strand length at equilibrium. The position of the slip-link obeys a Langevin-type equation of motion,

79 in which the force balance is considered among the drag force, osmotic force, tension acting on

80 diverging strands, and the random force. The chain sliding is described by a rate equation for the

81 number of Kuhn segments on each strand. The transport rate of the Kuhn segments between

82 consecutive strands is calculated along the chain according to the force balance considered for the

83 slip-link position.

84

85 As summarized earlier[21–23], the PCN model is located in a niche between the tube[30–32] and the bead-

86 spring[33] models; namely, the unit of calculation is the entanglement segment, which is also used in

87 single-chain slip-link models[34–37]. Meanwhile, the multi-chain dynamics is calculated as performed

88 for the bead-spring simulations and the other coarse-grained models that prohibits chain crossing[33,38–

89 40]. The multi-chain nature of the model excludes the mean-field type assumptions for thermal[41–43] and

90 convective[44] constraint release. The disturbance from the affine deformation owing to the force

91 balance around the entanglement[45] is also considered. The multi-chain construction was followed by

92 multi-chain slip-spring models[46–49], in which many Rouse chains dispersed in a simulation box are

93 connected by virtual springs. Except for the level of coarse-graining, these multi-chain models exhibit

94 similar features to reproduce entangled polymer dynamics[50].

95

96 In this study, we examined the experiment reported by Roy and Roland[24] for a polyisobutylene (PIB)

97 melt ($M_w = 46,000$ and $M_w/M_n = 3.2$). From this value of M_w, we determined the number of

98 strands per chain was $Z_0 = 12$. This value of Z_0 means that the molecular weight carried by a single

99 network strand is $M_0 = M_w/Z_0 \sim 3800$. We note that M_0 is much smaller than the entanglement

100 molecular weight $M_e = 9400$[24]. This difference is due to the additional fluctuations implemented in

101 the PCN model[51,52]. We also note that the value of M_0 determines the unit of modulus, G_0, by the

102 dimensional analysis as $G_0 = \rho RT/M_0$, where ρ is the density. Although this relation works well for

103 monodisperse systems, in this specific study, G_0 was determined independently of M_0 to

104 accommodate for the effect of the molecular weight distribution (MWD) in the experiment[24], as shown

105 later. Nevertheless, for simplicity in the molecular analysis, we simulated the monodisperse system.

106 The simulations were performed with non-dimensional units, where the units of length, energy, and

107 time were chosen as the average strand length, a, thermal energy, $k_B T$, and the diffusion time for a

108 node, $\tau_0 = \zeta a^2/6 \, k_B T$. Here, ζ is the friction of the single node. The simulation box dimension was

109   16^3, which is sufficiently larger than the chain dimension even under fast shear. The end-to-end

110   distance $\sqrt{\langle \mathbf{R}^2 \rangle}$ was 3.7 at equilibrium, and 8.2 under the fastest shear among all examined shear

111   rates. The strand number density under equilibrium was 10. For this system, the Rouse time is given

112   as $\tau_R = Z_0{}^2/2\pi^2 = 7.3\tau_0$ according to a previous study[53]. The longest relaxation time for the

113   viscoelastic relaxation was obtained from the equilibrium simulation[50,54] as $\tau_d = 77\tau_0$. To resolve

114   the slight changes in stress, we performed 24 independent simulation runs for each condition for

115   different initial equilibrated configurations.

116

117   **RESULTS AND DISCUSSION**

118   **Comparison with the experimental results**

119   Figure 1 shows the linear viscoelasticity of the sample. Comparison between the experimental data

120   (symbols) and the simulation results (curves) gives the model parameters as G_0 = 0.174 MPa, and

121   τ_0 = 0.021 s. As we mentioned in the previous section, G_0 must generally be determined from M_0.

122   However, in this specific study, we optimized G_0 separately from M_0 to accommodate for the effects

123   of the MWD on the compliance (i.e., the crossover between G' and G''). The value of τ_0 was

124   determined to reproduce the longest relaxation mode.
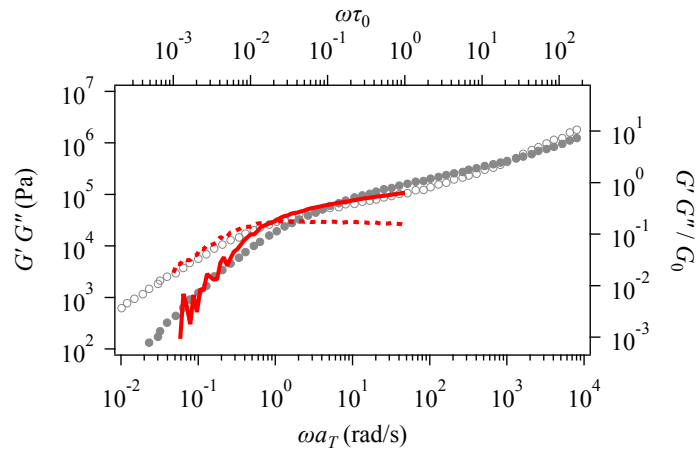
125

126   **Figure 1** Linear viscoelasticity. The filled and unfilled circles are the experimental data taken from

127   the literature[24]. The solid and broken curves are the simulation results.

128

129   Figure 2 shows the viscosity growth under start-up shear from equilibrium. The experimental data[24]

130   are shown for comparison. The simulation reproduces the viscosity overshoot and shear thinning only

131   qualitatively. In particular, the steady state viscosity is overestimated in the simulation. Similar

132   discrepancies have been reported even for monodisperse systems[25–29]. The tube model also has a

133   similar feature, and the mechanism of this discrepancy is unknown. Nevertheless, hereafter, we discuss

134   the response under 1 sec^{-1} in detail.

135
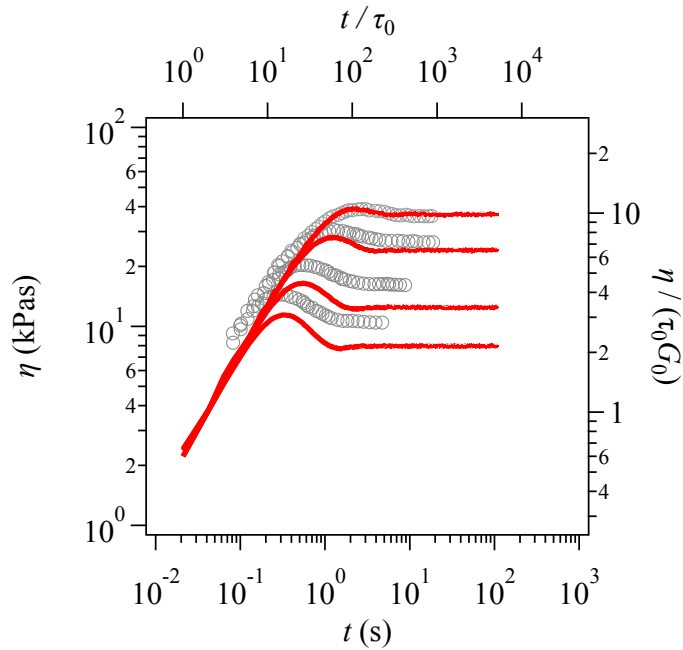
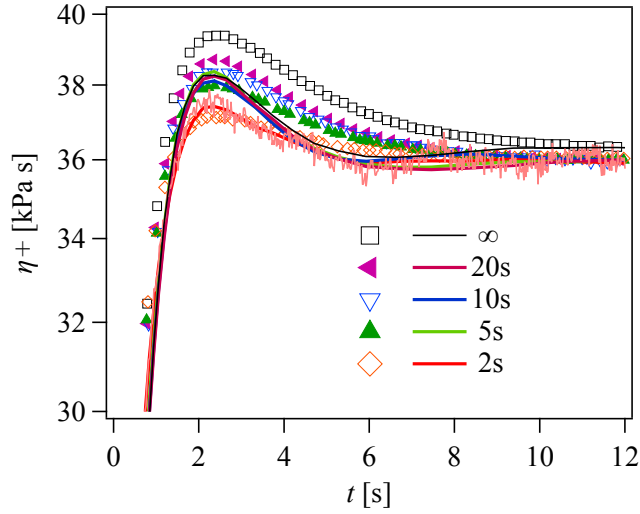**Figure 2** Viscosity growth under start-up shear at shear rates of 1, 2, 5 and 10 sec^{-1} from top to bottom. The solid curves and symbols represent the simulation and experimental results[24], respectively.

Figure 3 shows the viscosity growth under resumed shear at a shear rate of $1s^{-1}$. The prediction for the first start-up run (black curve) exhibits a discrepancy from the experimental data (black symbols) in this comparison. Indeed, the stress fluctuations in the simulation are concealed in the double-log plot in Figure 2, whereas they are visible in Figure 3 even after ensemble averaging for 24 independent simulation runs, as shown by the red thin curve for a rest time of 2 s. To extract the peak, we smoothed the simulation results using the second-order Savitzky-Golay method[55]. For the smoothed curves, the simulation qualitatively captures the experiment; namely, the magnitude of the viscosity overshoot increases with increasing rest time to recover the behavior exhibited under initial shear. Possibly owing to the MWD, the simulated viscosity decreases to a steady value faster than the experimental one.
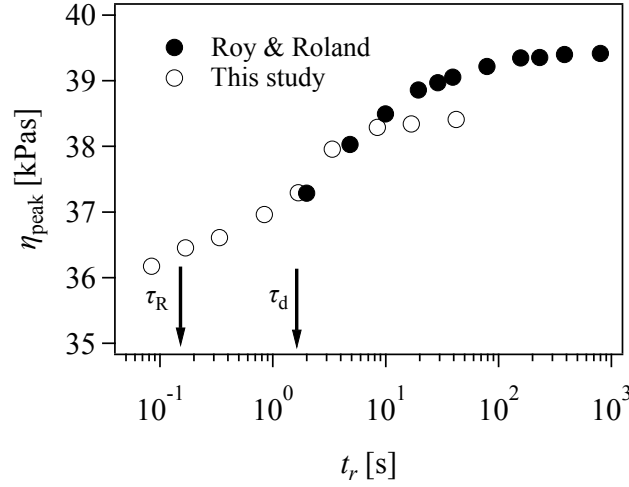
Figure 3 Viscosity growth under resumed shear at a shear rate of 1s^{-1} for various rest times after the initial shear. The data for the initial startup run are shown as an infinite rest time. The bold curves are the smoothed simulation results. The thin curve is the result for a rest time of 2s without smoothing. The symbols indicate the experimental results from the literature[24].

Figure 4 shows the peak value of the viscosity plotted as a function of the rest time, t_r. The viscoelastic relaxation time ($\tau_d = 77\tau_0 = 1.6$ s) and the Rouse time ($\tau_R = 7.3\tau_0 = 0.15$ s) for the simulation are indicated for comparison. The experimental data are not available for short t_r possibly due to experimental limitations. Consequently, direct comparison can only be made within a limited range of t_r. Nevertheless, the simulation reproduces the experiment reasonably well when $t_r \sim \tau_R$, where the peak value increases with increasing t_r to reach the same value as under the initial shear. However, for $t_r > \tau_d$, the viscosity overshoot is insensitive to t_r in the simulation, whereas it increases with t_r in the experiment. This difference is probably due to the MWD, which is neglected in the simulation.

Figure 4 Peak value of the viscocity overshoot under resumed shear as a function of rest time at a shear rate of 1sec^{-1}. The filled and unfilled symbols are the experimental[24] and simulation results, respectively. The viscoelastic relaxation time and the Rouse time for the simulation are indicated for comparison.

Decoupling analysis

We carried out molecular analysis based on the decoupling approximation[13], which is widely used for molecular constitutive equations;

$$\sigma = \frac{3}{V}\sum r_x r_y \approx 3\nu\lambda^2 S \qquad (1)$$

Here, σ is the shear stress, and the sum is taken for all the strands in the simulation box with volume V. $\mathbf{r} \equiv (r_x, r_y, r_z)$ is the strand vector, ν is the strand number density, $\lambda^2 (\equiv \langle \mathbf{r}^2 \rangle)$ is the average strand stretch, and $S(\equiv \langle (r_x r_y)/\mathbf{r}^2 \rangle)$ is the average strand orientation.

Figure 5 shows the transient behavior of the aforementioned molecular quantities under the resumed shear for various t_r/τ_0 values at shear rates of 10sec^{-1} and 1sec^{-1}. Note that we hereafter discuss the segment number per chain, Z, instead of ν hereafter. As shown in Fig 3, the magnitude of stress overshoot decreases with an increase of t_r. Being consistent with the stress-optical rule, the orientation exhibits a similar behavior. For a shear rate of 10 s^{-1} ($Wi_d = 16$) (Figure 5; left panels), the stretch contributes to the stress to delay the peak position from that of the orientation. The segment number develops similarly to the stretch, but the magnitude of change is much smaller than that for the stretch. Specifically, λ^2 increased by about 100% (Fig 5, purple line in the second panel from the bottom on the left), whereas the change for Z is less than 20%. The situation is similar for lower strain rates. We note that λ^2 does not start from unity even when the rest time is sufficiently long. Indeed, in our code, λ^2 is slightly (~10%) larger than unity at equilibrium because of the artificial

191 stiffness induced by a numerical cut-off for the monomer number on each strand.

192

193 Figure 5 (right panels) shows the case of $\dot{\gamma}$ =1 s^{-1} ($Wi_{\mathrm{d}} = 1.6$), where the stress is dominated by the

194 orientation, and the changes for λ^2 and Z are less pronounced. Consequently, the stress overshoot

195 is dominated by the orientation, and the strand density plays a secondary role. This result is consistent

196 with that of Ianniruberto and Marrucci[17], who qualitatively reproduced the interrupted shear response

197 using a tube model without chain stretch and variable entanglement density.

198
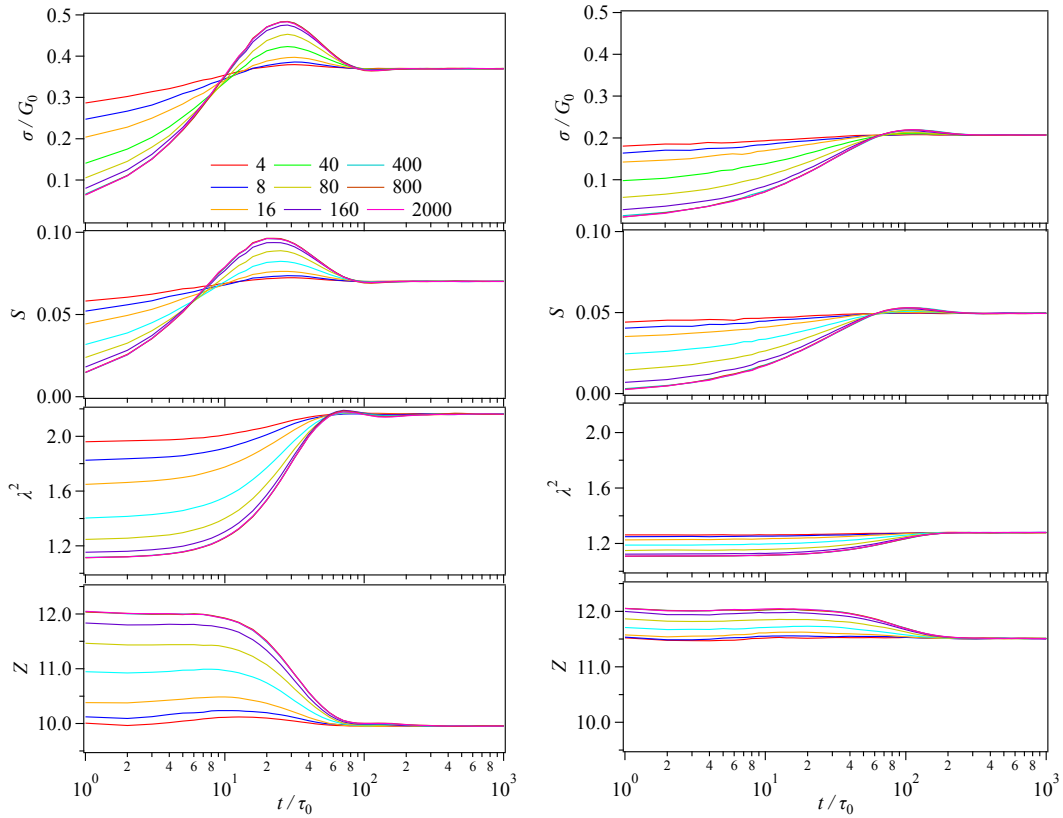
199

200 **Figure 5** Time development of stress, orientation, stretch, and segment number per chain (from top to

201 bottom) under resumed shear. The shear rates are 10 s^{-1} (left panel) and 1s^{-1} (right panel). The

202 normalized rest time (t_r/τ_0) is indicated in the figure. Note that the curves for rest times longer than

203 400 ($\gg \tau_{\mathrm{d}}$) overlap.

204

Structural relaxation during the rest

206 We now discuss whether the recovery of stress overshoot under resumed shear reflects structural

207 relaxation during the rest after the initial shear. Although the stress overshoot is dominated by the

208 orientation under resumed shear, as seen in Figure 5, the magnitude of overshoot may correlate with

209 the relaxation of other molecular characteristics.

211   Figure 6 shows the relaxation of stress and molecular characteristics after the initial shear. The

212   orientational relaxation is similar to the stress relaxation, which decays to zero during τ_d. The stretch

213   decreases to an equilibrium value reflecting the chain contraction, and the longest relaxation time is

214   comparable to τ_d rather than τ_R. The number of entanglements per chain recovers from a reduced

215   value, and the recovery time is close to τ_d. We note that in the original CCR theory[44,56], the

216   entanglement density is assumed to be constant, whereas the entanglement renewal is accelerated

217   under shear. However, molecular simulations[27,57–59] have revealed that the entanglement density

218   decreases under fast flows as a consequence of CCR.

219

220   One may argue that the relaxation time of stretch would be τ_R rather than τ_d. However, we note that

221   the contraction with τ_R is considered for the contour length in the tube theory[30], and not for each

222   segment. Indeed, even for our model, the relaxation time of the contour length is τ_R, as reported

223   previously[18]. Meanwhile, for the segment stretch, a retarded contraction has been reported[60,61]. This

224   retardation is due to the reduced number of entanglements as a result of CCR, as mentioned above.

225   When a fast and large deformation results in disentanglements, the number of Kuhn steps on each

226   strand becomes larger than the equilibrium value. In such a configuration, the tension acting on each

227   strand becomes weaker, thereby slowing contraction. Because the entanglement density recovers its

228   equilibrium state via reptation, the relaxation time of segment stretch is close to τ_d rather than τ_R[60,61].
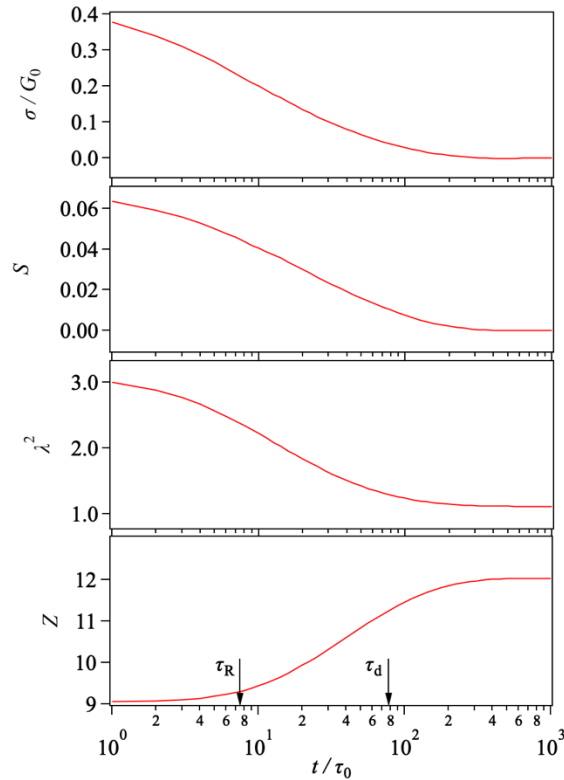
230　　**Figure 6** Relaxation from the steady state under a shear rate of 10 s^{-1} for stress, segment orientation,

231　　segment stretch, and segment number per chain from top to bottom.

232

233　　To compare the relaxation behaviors in Figure 6 with each other, we define the relaxation functions as

234　　follows:

$$\varphi_\sigma(t) = A_\sigma \sigma(t) \qquad\qquad (2)$$

$$\varphi_S(t) = A_S S(t) \qquad\qquad (3)$$

$$\varphi_\lambda(t) = A_\lambda(\lambda^2(t) - 1) \qquad\qquad (4)$$

$$\varphi_Z(t) = A_Z(1 - Z(t)/Z_0) \qquad\qquad (5)$$

239　　Figure 7 shows the relaxation functions plotted with the normalized linear relaxation modulus

240　　$G(t)/G_0$. The parameters in Eqs 2-5, A_σ, A_S, A_λ and A_Z, were chosen to match the functions with

241　　$G(t)/G_0$ for $t \geq \tau_d$; these parameters depend on the shear rate. In this regime, all relaxation

242　　functions overlap with $G(t)/G_0$ (broken curve) showing the identical relaxation time of τ_d. In the

243　　short-time range ($t < \tau_d$), most of the relaxation functions depend on the shear rate. Because of the

244　　non-linearity imposed by the shear, the stress relaxation, $\varphi_\sigma(t)$ (red curve), does not coincide with

245　　$G(t)$, and the intensity of the fast relaxation modes increases with an increase of shear rate. Similar

246　　behavior is seen for the orientational relaxation, $\varphi_S(t)$ (yellow curve), which overlaps with $\varphi_\sigma(t)$

247　　for low shear rates; this similarity is consistent with the stress-optical rule. Meanwhile, for high shear

248　　rates, the orientational relaxation becomes much lower than $\varphi_\sigma(t)$ owing to the contribution of

249　　stretch. The stretch relaxation $\varphi_\lambda(t)$ (green curve) shows a growth of the intensity for fast relaxation

250　　modes for fast shear rates due to the chain stretch. $\varphi_Z(t)$ (blue curve) is almost insensitive to the

251　　shear rate. Interestingly, only for this relaxation function, fast modes do not appear, even for high shear

252　　rates. This behavior can be rationalized if the recovery of Z is dominated by reptation motion as

253　　assumed in the tube theory[30]. Furuichi et al.[60] have reported such behavior for PCN simulations under

254　　large step shear deformations.

255

256　　We now compare the relaxation function and the recovery of stress overshoot under resumed shear.

257　　From the recovery behavior shown in Figure 4, we define the mitigation function, M_η, for the recovery

258　　of viscosity overshoot as a function of t_r as

$$M_\eta(t_r) = B_\eta\big(1 - \eta_{\text{peak}}(t_r)/\eta_{\text{peak}}(\infty)\big) \qquad (6)$$

260　　Here, B_η is a numerical constant that depends on the shear rate. Assuming that t_r and the relaxation

261　　period in Figure 5 are compatible, we plot M_η (unfilled circles in Figure 7) with a value of B_η that

262　　attains reasonable comparison between M_η and the relaxation functions. Note that the value of M_η

263　　is not available for the lowest shear rate, because we did not observe any overshoot for this case. For

264　　the other shear rates, M_η is close to φ_Z, and these two functions are almost insensitive to the shear

265　　rate, exhibiting no growth of the intensity for fast relaxation modes. To be fair, we note that there is

266   considerable uncertainty for M_η under low shear rates.

267

268   One may argue that similar mitigation functions could be defined for the molecular quantities as well.

269   However, such an analysis is not straightforward. For example, as seen in Figure 4, there is no peak

270   for Z. For λ^2, although a faint peak is observed, it is not located at the same position as that for η. As

271   mentioned above, S behaves similarly to η. However, the peak positions do not coincide at high

272   shear rates owing to the contributions of Z and λ^2 to the stress.

273

274
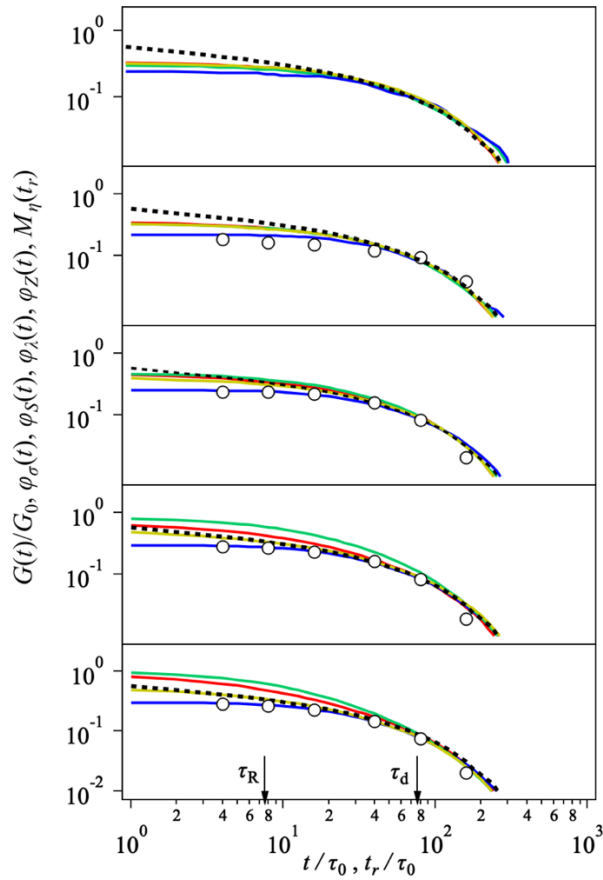
Figure 7 Relaxation functions for stress (red), orientation (yellow), stretch (green), and entanglement
density (blue), as defined in Eqs. 2-5. The linear relaxation modulus is shown by the broken curve.
The mitigation function for the viscosity overshoot defined by Eq. 6 is marked with open circles. The
shear rates are 0.5, 1, 2, 5, and 10 s^{-1} from top to bottom. The Rouse time and the longest relaxation
time are indicated by the arrows.

280

281   Figure 8 shows the numerical constants A and B in Eqs. 2-6 plotted as functions of the shear rate. A_σ

282   (red) and A_S (yellow) are almost insensitive to the shear rate, whereas A_λ (green) and A_Z (blue)

283 decrease with an increase of the shear rate in a power-law manner, for which the exponent is

284 approximately -1. For the mitigation function, M_η, B_η (black) exhibits a similar decay to A_λ and

285 A_Z. These shear rate dependence of A_λ, A_Z and B_η suggest a linear response for the longest

286 relaxation mode of $\varphi_\lambda(t)$, $\varphi_Z(t)$ and $M_\eta(t_r)$.

287

288
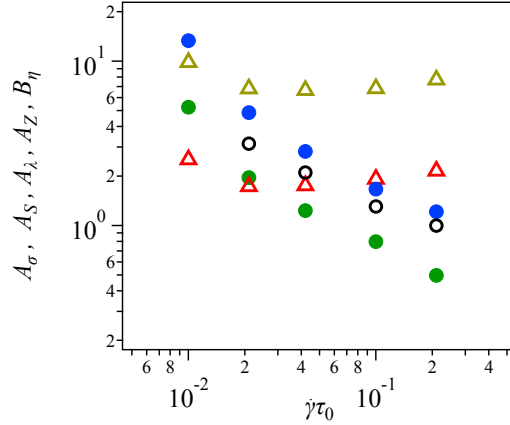
289

290 **Figure 8** Numerical constants defined for Eqs. 2-6 plotted as functions of the normalized shear rate.

291 A_σ and A_S are represented by unfilled triangles in red and yellow, and A_λ and A_Z are indicated

292 by filled circles in green and blue, respectively. B_η is represented by black unfilled circles.

293

294

295 The similarities between φ_Z and M_η seen in Figures 7 and 8 are unexpected, and we are unable to

296 provide a reasonable explanation for this behavior. We emphasize that the magnitude of the overshoot

297 is not measured for the system during the relaxation. Rather, the overshoot reflects a transient state

298 between a partly relaxed state and a non-equilibrium state under steady shear. Because of this

299 fundamental difference between the relaxation functions and the mitigation function, the results in

300 Figures 7 and 8 cannot be explained by conventional molecular pictures.

301

302 We note that the presented results may be related to the model settings and the algorithm used in the

303 conducted simulation, and that other models may give different results. Indeed, because the definition

304 of entanglement is model dependent, the entanglement density and its response to deformations are

305 also model dependent. For example, as mentioned in the Introduction, Ianniruberto and Marrucci[17]

306 argued that the response to interrupted shear can be qualitatively described using a the tube model,

307 whereby the entanglement density is insensitive to deformations. Even among models that assume the

308 entanglement density is reduced under fast and large deformations, the magnitude of entanglement

309 reduction is not universal[59,61]. Meanwhile, we note the network statistics assumed in the PCN model

310 is consistent with the topological network extracted from atomistic molecular simulations[62,63]. In this

311 respect, the presented results would reflect the dynamics of the topological network in some extent.

312

313 We also note that some experimental studies suggest flaws in the conventional modeling of

314 entanglement. For exapmle, for the dielectric measurement of polyisoprene under steady shear,

315 Watanabe et al. [64,65] have reported that the relaxation time and the relaxation intensity measured in the

316 shear gradient direction do not depend on the shear rate. This result means that the end-to-end

317 dimension and its fluctuations along the shear gradient direction do not change, even under fast shear,

318 even when the viscosity shows the shear thinning. To the best of our knowledge, conventional

319 molecular theories cannot reproduce this behavior[25,27]. Teixeira et al. [66] have conducted a direct

320 observation of single DNA molecules under start-up shear. They compared the observed

321 conformational change with that predicted by the tube theory, and found that the observed DNA

322 response is much slower than the theoretical one. PCN simulations failed to reproduce this result as

323 well, even though the viscosity growth was in quantitative agreement[67]. These flaws mean that the

324 conventional molecular theories may not be compatible with the conformational dynamics of polymers,

325 even though they have achieved remarkable success for describing the rheological response of

326 polymers. In this respect, molecular modeling of entanglement is still a challenge, and further

327 improvement is necessary for the conventional models, including PCN. The commonly applied

328 assumptions, such as the homogeneous deformation and the binary contact at the entanglement point,

329 might be problems that should be addressed in future investigations.

330

331 **CONCLUSIONS**

332 We performed multi-chain slip-link simulations for an entangled polymer under interrupted shear. The

333 simulation reproduced the experimental data for the recovery of viscosity overshoot as a function of

334 rest time. Owing to this agreement, we analyzed the molecular behavior following the decoupling

335 approximation. From the results, we reasonably confirmed that the overshoot is mainly due to segment

336 orientation. To determine if the recovery of the overshoot is related to structural relaxation during the

337 rest after the initial shear, we observed the relaxation of segment orientation, segment stretch, and

338 entanglement density. We compared these relaxation functions with the mitigation of the viscosity

339 overshoot, assuming that the waiting time before the resumed flow is compatible to the relaxation

340 period. The comparison revealed that the mitigation of viscosity overshoot is similar to the relaxation

341 of entanglement density. The similarity between the mitigation of overshoot and the relaxation of

342 entanglement is nontrivial, and might be model-dependent. The effects of the molecular weight

343 distribution would be worth investigating as well. We are currently conducting researches in these

344 directions and the results will be reported elsewhere.

345

REFERENCES

1   J. D. Huppler, I. F. Macdonald, E. Ashare, T. W. Spriggs, R. B. Bird and L. A. Holmes, *Trans. Soc. Rheol.*, 1967, **11**, 181–204.

2   R. A. Stratton and A. F. Butcher, *J. Polym. Sci. Part A-2 Polym. Phys.*, 1973, **11**, 1747–1758.

3   A. V. Tobolsky and R. D. Andrews, *J. Chem. Phys.*, 1945, **13**, 3–27.

4   M. S. Green and   a. V. Tobolsky, *J. Chem. Phys.*, 1946, **14**, 80.

5   W. W. Graessley, *J. Chem. Phys.*, 1965, **43**, 2696–2703.

6   M. Doi and S. F. Edwards, *J. Chem. Soc. Faraday Trans. 2*, 1978, **74**, 1802.

7   J. M. Dealy and W. K.-;W. Tsang, *J. Appl. Polym. Sci.*, 1981, **26**, 1149–1158.

8   E. Menezes and W. Graessley, *J. Polym. Sci. Polym. Phys. Ed.*, 1982, **20**, 1817–1833.

9   J. Sanchez-Reyes and L. A. Archer, *J. Rheol. (N. Y. N. Y).*, 2003, **47**, 469–482.

10   C. G. Robertson, S. Warren, D. J. Plazek and C. M. Roland, *Macromolecules*, 2004, **37**, 10018–10022.

11   S. Q. Wang, Y. Wang, S. Cheng, X. Li, X. Zhu and H. Sun, *Macromolecules*, 2013, **46**, 3147–3159.

12   P. G. Santangelo and C. M. Roland, *J. Rheol. (N. Y. N. Y).*, 2001, **45**, 583–594.

13   D. S. Pearson, A. D. Kiss, L. J. Fetters and M. Doi, *J. Rheol. (N. Y. N. Y).*, 1999, **33**, 517–535.

14   Y. Masubuchi and H. Watanabe, *ACS Macro Lett.*, 2014, **3**, 1183–1186.

15   J. Cao and A. E. Likhtman, *ACS Macro Lett.*, 2015, **4**, 1376–1381.

16   Y. Masubuchi and H. Watanabe, *Nihon Reoroji Gakkaishi*, 2016, **44**, 65–68.

17   G. Ianniruberto and G. Marrucci, *ACS Macro Lett.*, 2014, **3**, 552–555.

18   M. Doi and S. F. Edwards, *J. Chem. Soc. Faraday Trans. 2*, 1978, **74**, 1818.

19   R. S. Graham, E. P. Henry and P. D. Olmsted, *Macromolecules*, 2013, **46**, 9849–9854.

20   Y. Masubuchi, J.-I. Takimoto, K. Koyama, G. Ianniruberto, G. Marrucci and F. Greco, *J. Chem. Phys.*, 2001, **115**, 4387–4394.

21   Y. Masubuchi, *Annu. Rev. Chem. Biomol. Eng.*, 2014, **5**, 11–33.

22   Y. Masubuchi, in *Computer Simulation of Polymeric Materials*, Springer Singapore, Singapore, 2016, pp. 101–127.

23   Y. Masubuchi, in *Reference Module in Materials Science and Materials Engineering*, Elsevier, 2016, pp. 1–7.

24   D. Roy and C. M. Roland, *Macromolecules*, 2013, **46**, 9403–9408.

382   25   Y. Masubuchi, H. Watanabe, G. Ianniruberto, F. Greco and G. Marrucci, *Nihon Reoroji*
383   *Gakkaishi*, 2004, **32**, 197–202.

384   26   T. Yaoita, T. Isaki, Y. Masubuchi, H. Watanabe, G. Ianniruberto and G. Marrucci,
385   *Macromolecules*, 2012, **45**, 2773–2782.

386   27   T. Uneyama, Y. Masubuchi, K. Horio, Y. Matsumiya, H. Watanabe, J. A. Pathak and C. M.
387   Roland, *J. Polym. Sci. Part B Polym. Phys.*, 2009, **47**, 1039–1057.

388   28   Y. Masubuchi, G. Ianniruberto and G. Marrucci, *Nihon Reoroji Gakkaishi*, 2018, **46**, 23–28.

389   29   Y. Masubuchi, G. Ianniruberto and G. Marrucci, *Soft Matter*, 2020, **16**, 1056–1065.

390   30   M. Doi and S. F. Edwards, *The Theory of Polymer Dynamics*, Clarendon press, Oxford, 1986.

391   31   D. W. Mead, R. G. Larson and M. Doi, *Macromolecules*, 1998, **31**, 7895–7914.

392   32   R. S. Graham, A. E. Likhtman, T. C. B. McLeish and S. T. Milner, *J. Rheol. (N. Y. N. Y).*, 2003,
393   **47**, 1171.

394   33   K. Kremer and G. S. Grest, *J. Chem. Phys.*, 1990, **92**, 5057.

395   34   C. C. Hua and J. Schieber, *J. Chem. Phys.*, 1998, **109**, 10018–10027.

396   35   J. D. Schieber, J. Neergaard and S. Gupta, *J. Rheol. (N. Y. N. Y).*, 2003, **47**, 213.

397   36   M. Doi and J. -i. Takimoto, *Philos. Trans. R. Soc. London Ser. A-Mathematical Phys. Eng. Sci.*,
398   2003, **361**, 641–650.

399   37   S. Shanbhag, R. G. Larson, J. Takimoto and M. Doi, *Phys. Rev. Lett.*, 2001, **87**, 195502.

400   38   A. Baumgartner and K. Binder, *J. Chem. Phys.*, 1981, **75**, 6.

401   39   J. T. Padding and W. J. Briels, *J. Chem. Phys.*, 2001, **115**, 2846.

402   40   S. Kumar and R. G. Larson, *J. Chem. Phys.*, 2001, **114**, 6937.

403   41   J. des Cloizeaux, *Europhys. Lett.*, 1988, **5**, 437–442.

404   42   W. Graessley, *Adv. Polym. Sci.*, 1982, **47**, 67–117.

405   43   C. Tsenoglou, *ACS Polym. Prepr.*, 1987, **28**, 185–186.

406   44   G. Marrucci, *J. Nonnewton. Fluid Mech.*, 1996, **62**, 279–289.

407   45   G. Marrucci, F. Greco and G. Ianniruberto, *Macromol. Symp.*, 2000, **158**, 57–64.

408   46   T. Uneyama and Y. Masubuchi, *J. Chem. Phys.*, 2012, **137**, 154902.

409   47   V. C. Chappa, D. C. Morse, A. Zippelius and M. Müller, *Phys. Rev. Lett.*, 2012, **109**, 148302.

410   48   A. Ramírez-Hernández, F. A. Detcheverry, B. L. Peters, V. C. Chappa, K. S. Schweizer, M.
411   Müller and J. J. de Pablo, *Macromolecules*, 2013, **46**, 6287–6299.

412   49   M. Langeloth, Y. Masubuchi, M. C. Böhm and F. Müller-plathe, *J. Chem. Phys.*, 2013, **138**,
413   104907.

414   50   Y. Masubuchi and T. Uneyama, *Soft Matter*, 2018, **14**, 5986–5994.

415   51   Y. Masubuchi, G. Ianniruberto, F. Greco and G. Marrucci, *J. Chem. Phys.*, 2003, **119**, 6925–
416   6930.

417   52   Y. Masubuchi, G. Ianniruberto, F. Greco and G. Marrucci, *J. Nonnewton. Fluid Mech.*, 2008,

418   **149**, 87–92.

419   53   K. Furuichi, C. Nonomura, Y. Masubuchi, H. Watanabe, G. Ianniruberto, F. Greco and G.

420   Marrucci, *Rheol. Acta*, 2008, **47**, 591–599.

421   54   Y. Masubuchi, *Nihon Reoroji Gakkaishi(Journal Soc. Rheol. Japan)*, 2020, **48**, 37–42.

422   55   A. Savitzky and M. J. E. Golay, *Anal. Chem.*, 1964, **36**, 1627–1639.

423   56   G. Ianniruberto and G. Marrucci, *J. Nonnewton. Fluid Mech.*, 1996, **65**, 241–246.

424   57   C. Baig, P. S. Stephanou, G. Tsolou, V. G. Mavrantzas and M. Kröger, *Macromolecules*, 2010,

425   **43**, 8239–8250.

426   58   Y. Masubuchi, *J. Chem. Phys.*, 2015, **143**, 224905.

427   59   A. P. Sgouros, G. Megariotis and D. N. Theodorou, *Macromolecules*, 2017, **50**, 4524–4541.

428   60   K. Furuichi, C. Nonomura, Y. Masubuchi and H. Watanabe, *J. Chem. Phys.*, 2010, **133**, 174902.

429   61   Y. Masubuchi, *Polymers (Basel).*, 2019, **11**, 370.

430   62   Y. Masubuchi, T. Uneyama, H. Watanabe, G. Ianniruberto, F. Greco and G. Marrucci, *J. Chem.*

431   *Phys.*, 2010, **132**, 134902.

432   63   T. Uneyama and Y. Masubuchi, *J. Chem. Phys.*, 2011, **135**, 184904.

433   64   H. Watanabe, S. Ishida and Y. Matsumiya, *Macromolecules*, 2002, **35**, 8802–8818.

434   65   K. Horio, T. Uneyama, Y. Matsumiya, Y. Masubuchi and H. Watanabe, *Macromolecules*, 2014,

435   **47**, 246–255.

436   66   R. E. Teixeira, A. K. Dambal, D. H. Richter, E. S. G. Shaqfeh and S. Chu, *Macromolecules*,

437   2007, **40**, 2461–2476.

438   67   Y. Masubuchi, K. Furuichi, K. Horio, T. Uneyama, H. Watanabe, G. Ianniruberto, F. Greco and

439   G. Marrucci, *J. Chem. Phys.*, 2009, **131**, 114906.

440

441

16
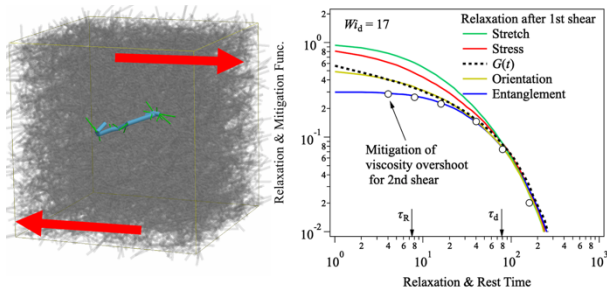
442
443
444   TOC graphic:

445

446   In slip-link simulations, recovery of viscosity overshoot in interrupted shear reflects relaxation of
447   entanglement density during interval

448
449